# Redistribution of Minor and Trace Elements During Roasting of Cu-Rich Complex Concentrate in Inert Atmosphere

PANDE NISHANT PRASAD, HELEN THOMAS, ANDREAS LENNARTSSON, and CAISA SAMUELSSON

A Cu-rich polymetallic complex concentrate produced at the Garpenberg Mines of Boliden Mineral AB, Sweden is investigated. Roasting at 700 °C in N_2 leads to extensive liquid formation. The calcine obtained after cooling down to the room temperature is found to be severely sintered, entrapping numerous melt nuggets. This work focuses on analyzing redistribution of the minor (Ag) and trace elements consequent to the roasting treatment. Advanced micro-analytical techniques such as quantitative evaluation of minerals by scanning electron microscopy (QEMSCAN), laser-ablation inductively coupled plasma-mass spectrometry (ICP-MS) and scanning electron microscopy-energy dispersive X-ray spectroscopy (SEM-EDS) are used in conjunction for detailed characterization of the initial concentrate and the roasted calcine, especially the melt nuggets (which symbolizes the phases which were molten at 700 °C). The minor element—Ag is primarily in the silver-antimonide and tetrahedrite mineral phases in the initial concentrate. Ag separates out of tetrahedrite when the later interacts with galena to form a liquid phase. Furthermore, Mn, Cd, Tl and Hg are the relevant trace elements in the Garpenberg concentrate. Sphalerite is the major host of Mn, Cd and Hg. Tl is mainly in galena. Consequent to liquid formations at 700 °C, the trace elements redistribute and tend to segregate in low-melting phase-fractions. Statistical methods such as correlation matrices and clustering analysis are used effectively in evaluating the data from laser-ablation ICP-MS measurements on sulphide samples.

Graphical Abstract
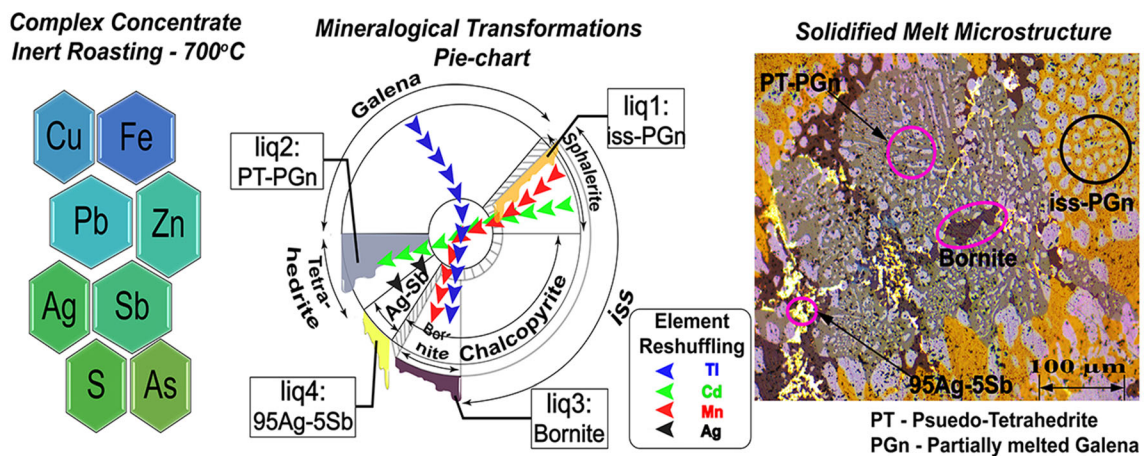
© The Author(s) 2022

PANDE NISHANT PRASAD, ANDREAS LENNARTSSON, and CAISA SAMUELSSON are with the Luleå Tekniska Universitet, 97187, Luleå Sweden. Contact e-mail: pande.nishant.prasad@ltu.se HELEN THOMAS is with the Boliden Mineral AB, 93681, Boliden, Sweden.

I. INTRODUCTION

TREATMENT of polymetallic Cu-rich complex concentrates (containing multiple other elements such as Pb, Zn, Ag, As, Sb) in a conventional smelting-converting route of Cu-extraction is difficult. Currently, these complex concentrates are utilized by blending in small proportions with simpler concentrates which chiefly comprise of chalcopyrite, pyrite and some non-sulphide gangues. Such minor proportions of complex concentrates in the input feed are dictated by the process-limitations for producing high purity Cu as the end-product. However, due to rampant depletion of simpler chalcopyrite-pyrite-based Cu-deposits, there is now an increased urgency to develop novel Cu-extraction processes which can accept feeds high in complex concentrates. Besides, Cu is indispensable for the manufacturing of electric vehicles and components related to wind-, solar-, hydro-power and batteries. The demand for copper is going to increase dramatically, owing to the prevalent all-around emphasis on cleaner energy production. Therefore, a more efficient utilization of mined Cu resources including the Cu-rich complex concentrates is essential.

Roasting is a vital step which offers partial volatilization of certain deleterious elements such as As and Sb from the feed concentrate.[1–10] Secondly, the reactions during roasting are mainly gas-solid and solid-solid. Consequently, the resultant calcine would still be heterogeneous with relatively distinguishable phases (element-wise) unlike in the subsequent smelting-converting stages involving homogeneous liquid phases (slag/matte/metal). Therefore, further research could evolve roasting as one of the possible upgradation steps of complex concentrates for increasing their utility in the Cu pyrometallurgical extraction. Experimental investigations of roasting complex concentrates in controlled environments for studying the mineralogical transformations and possible elemental redistributions would cater to such objectives.

Previous studies on high temperature sulphide mineralogical interactions can be found mainly in the geological literature, elucidating the various aspects of mineralization.[11–20] Our recent publications reported the observations related to sulphide mineralogical interactions in context of roasting, based on the experiments performed with Cu-rich complex concentrates.[21–23] Pertinent findings from the geological literature such as the existence of solid-solution phases in the CuS-ZnS-FeS system[12,13] and liquid phases in the PbS-CuS-Sb$_2$S$_3$ system[14,15] could very well explain the mineralogical transformations observed during the roasting of multiple complex concentrates.

Furthermore, the sulphide minerals have been extensively studied by the geologists for hosting certain precious metals and critical elements.[24–33] The relative partitioning of these elements during the co-crystallization of the sulphide minerals[34,35] and between sulphide and silicate assemblages[36] have also been elaborated. Similar to the mineral crystallizations in ore bodies, roasting of complex concentrates also involves the

formation of new solid and liquid phases.[21,22] Such physicochemical changes can stimulate redistribution of the minor and trace elements, originally residing in distinct mineral phases in the complex concentrate. Detailed characterization of complex concentrates together with their roasted calcine to determine the elemental redistributions is missing, which is the focus of the current study. Such studies could be useful in developing new strategies for the economic extraction of scarcely occurring critical elements. Additionally, in light of the catalytic effects of certain trace elements in mineralogical transformations,[37] determination of their inter-phase mobility in roasting conditions could be a valuable scientific information.

In this work, various micro-analytical techniques such as SEM-EDS, QEMSCAN and Laser-Ablation ICP-MS (LA-ICP-MS) are used collectively to determine mineralogical transformations and elemental distributions. The aim is to determine the trends for mobilization of the minor and trace elements consequent to laboratory-scale roasting. The experiment is performed in Nitrogen atmosphere with slight impurities (O_2 < 5 ppm, H_2O < 5 ppm, $p^{O_2} \approx 10^{-5.3}$ bar). Such conditions would facilitate a fundamental study on the mineral assemblies in weakly oxidizing roasting conditions.

LA-ICP-MS is a proven method for effective characterization of trace elements. However, there are known challenges in accurate determination of element concentrations through this method for the sulphide samples.[38,39] Considering such limitations, the measurement data from LA-ICP-MS are directly used for cluster analysis without further quantification. Clustering has been used previously for deduction of vital sample-related features from the LA-ICP-MS data.[40–43] Results from the clustering approach followed in this article are appropriately validated, suggesting that the LA-ICP-MS measurement on sulphide samples is good enough for sound statistical analysis, if not for reliable quantification.

II. EXPERIMENT

A. *Materials and Methods*

A Cu-rich polymetallic complex concentrate produced from Garpenberg Mines by Boliden Mineral AB, Sweden was used in this study. Chemical composition of this concentrate is stated in Table I.

10 g of 38 to 53 μm size fraction of this concentrate was heated in a vertical tube furnace up to a temperature of 700 °C in N_2 atmosphere (referred to as 'non-isothermal' roasting in Prasad *et al.*[21], N_2 flow rate = 5 l/min). This narrow size-band was chosen to estimate the post-treatment particle-size alterations during microscopic investigations. A schematic of the experimental setup is shown in Figure 1(a). The concentrate experienced a heating rate of 4 °C/min, 60 minutes holding at 700 °C and 3 °C/min cooling rate. Also, the roasted calcine displayed in Figure 1(b) suggests that there was substantial melt formation. The roasted residue consisted of numerous solidified sulphide-melt nuggets

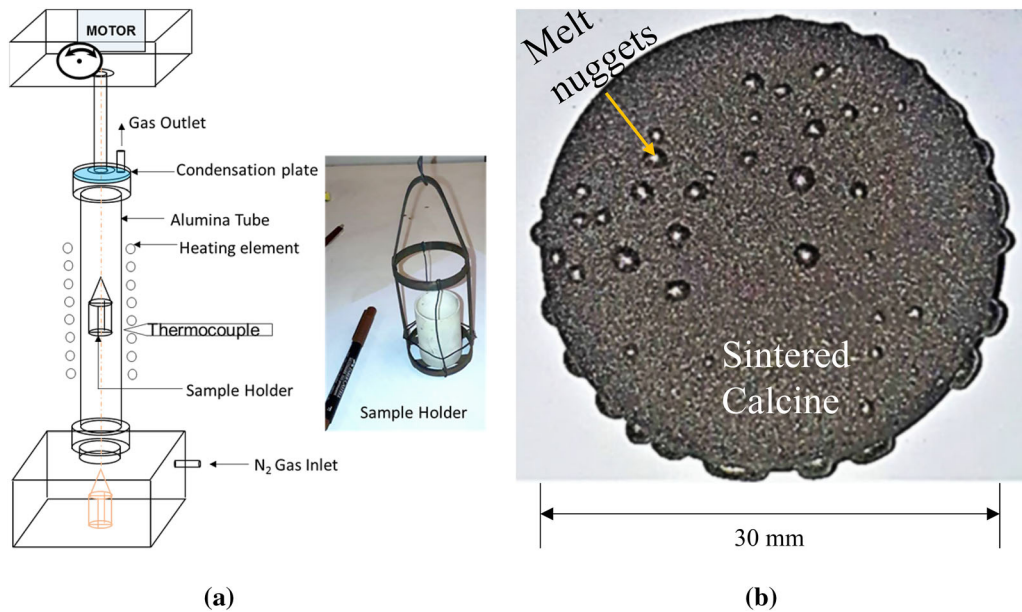| Concentrate/Element (Wt Pct)	Cu	Zn	Pb	Fe	Si	Mg	S	Ag	As	Sb
Garpenberg	19.3	9.5	15.3	19.8	0.8	0.2	26.1	1.82	0.23	2.04

Data from Prasad et al.[21]

Fig. 1—(a) Schematic of the vertical tube furnace experimental setup, also showing an actual image of the sample holder (alumina crucible); (b) Image of the sintered calcine and entrapped melt nuggets, suggesting liquid formation during heating at 700 °C. Reprinted from Prasad et al.[21] under the terms of Creative Commons CC BY license.

entrapped in the sintered calcine. The melt nuggets would constitute phases which were completely liquid at the reaction temperature. The initial concentrate and these melt nuggets were characterized in this study to analyze the effect of liquid formation during the high temperature mineralogical interactions. The mineral phases presented in the initial concentrate and the roasted products with their abbreviations as quoted in this article are listed in Table II.

B. Microanalytical Techniques

1. SEM/EDS

The initial concentrate (38-53 μm) and portions of the roasted calcine entrapping melt nuggets [shown in Figure 1(b)] were moulded in epoxy mounts. These polished and carbon coated epoxy mounts were examined in a Zeiss Merlin FEG SEM (Scanning Electron Microscope) having an Oxford Instruments X-Max EDS (Energy-Dispersive X-ray Spectroscopy) detector operated by AZtec software. The operating conditions included - working distance of 8.5 mm, probe current of 1nA and accelerating voltage of 20 kV. Beam measurement calibration was performed on pure copper. The EDS spot measurements for elemental composition were reported in mol. pct after normalization (Σ = 100 mol. pct). EDS-chemical mapping of certain portions of the melt-nugget microstructures were also performed.

2. Optical microscopy

The uncoated epoxy mounts were studied in an optical microscope, Axioscope 7 (Zeiss) with the provision of imaging large fields of view by 'tiling and stitching'. Full polished surface of the epoxy (diameter = 30 mm) comprising of the initial concentrate (38 to 53 μm) was scanned to generate a high-resolution optical image of the moulded concentrate particles. The melt nuggets microstructures were also imaged using this technique. The light intensity was manually adjusted to attain microstructural images with distinctly colored phases in the reflective mode of operation.

3. Automated quantitative mineralogical analysis (QEMSCAN)

The epoxy mount of the initial concentrate was additionally analysed in QEMSCAN (Model–QEMSCAN 650, FEI with W-filament and two Brukar XFlash 5030 EDS detectors) at Boliden Mineral AB, Boliden, Sweden. Details of this measurement are mentioned in Prasad et al.[22]

4. Laser-ablation ICP-MS

The initial concentrate and the melt-nugget microstructures were also analyzed in a Laser-Ablation ICP-MS (henceforth referred as LA-ICP-MS) setup. Details of the equipment and measurement specifications are presented in Table III.

Spot measurements were performed on individual particles of minerals (all base metal sulphides, tetrahedrite and silver-antimonide) in the initial concentrate (38 to 53 μm). The LA-ICP-MS setup provides visualization of the loaded sample surface only through an optical camera. Therefore, pre-determination of mineralogy of the particles was essential to know which mineral was ablated. This was done using the false-colored mineral image (from QEMSCAN) together with the optical image (from Axioscope microscope) of the entire polished surface of the epoxy. An illustration of such an exercise is shown in Figures 2(a) and (b) for identifying the sites of tetrahedrite in the initial concentrate. As shown in Figure 2(b), certain pores over the polished surface were used as visual references, Spots of specific minerals were identified in the near vicinity of these pores for the laser-ablation. Such LA-ICP-MS spot measurements were performed at 47 spots for tetrahedrite, 6 spots of chalcopyrite, 5 spots of sphalerite, 5 spots of galena, and 1 spot of silver-antimonide. Relatively higher number of spots of tetrahedrite were chosen considering the extensive variability in its composition (discussed later in Section III-B-1-b, Figure 13(b) of this article).

Also, notably only one spot-measurement was performed for the silver-antimonide (Ag-Sb) since it was difficult to distinctly identify this mineral phase. It existed mostly in complex association forms, as illustrated in Figure 3. It was possible to track just one particle containing this phase in the vicinity of the position-guiding pores, with mineral grain size greater than the laser spot-size of 25 μm.

For evaluating the characteristics of phases in the melt nuggets, element mapping method of LA-ICP-MS was used instead of the spot measurements. This method was chosen owing to the complexity in phase assemblage in the microstructure of the melt nuggets, comprising numerous intergrown phases (discussed later in Section III-B-1 of this article). A suitable rectangular area in the melt-nugget microstructure, featuring all the melt-fractions was ablated in 'rastering mode'. An optimally small spot-size of 10 μm was chosen for element mapping (compared to 25 μm in spot measurements). Further low spot-size could lead to problems of unacceptably low signal-to-noise ratio in the LA-ICP-MS measurement data.[44]

a. Element-list for LA-ICP-MS measurements 23 elements/isotopes were analyzed during the spot measurements and element-mapping - ^{34}S, ^{55}Mn, ^{57}Fe, ^{59}Co, ^{60}Ni, ^{65}Cu, ^{66}Zn, ^{69}Ga, ^{75}As, ^{82}Se, ^{95}Mo, ^{107}Ag, ^{111}Cd, ^{115}In, ^{118}Sn, ^{121}Sb, ^{125}Te, ^{182}W, ^{197}Au, ^{202}Hg, ^{205}Tl, ^{206}Pb, and ^{209}Bi. This list was replicated from the recent work of George *et al.*[35] wherein they performed LA-ICP-MS measurements on mineral assemblages involving the base metal sulphides (BMS) and complex minerals such as tetrahedrite. Similar combination of minerals existed in the complex Cu-rich Garpenberg concentrate studied in this work.

b. LA-ICP-MS measurement data-reduction The data of LA-ICP-MS spot measurements was processed in a time-resolved mass spectrometry software package— 'iolite 4' (© The iolite Team,[45]) for data-reduction. The signals of count/s (cps) corresponding to the time-period between 1 sec after 'Laser-start' till 5 sec prior to 'Laser-stop' in each laser-ablation cycle were selected for further analysis. This approach of data-reduction performed over the measured cps-signals for Ag in tetrahedrite belonging to the initial concentrate is illustrated in Figure 4. Notably, the procedure of 'background-subtraction' for the measurement data was bypassed, as it was resulting in numerous negative values of cps-signals in the reduced data, especially for the trace elements.

Table II. List of Mineral Phases and Their Abbreviations

Mineral	Abbreviation	Chemical Formula/Resemblance
Chalcopyrite	Ccp	$CuFeS_2$
Sphalerite	Sph	$(Zn,Fe)S$
Galena	Gn	PbS
Pyrite	Py	FeS_2
Tetrahedrite	Ttr	$(Cu,Ag,Fe,Zn)_{12}(Sb,As)_4S_{13}$
Silver-Antimonide	Ag-Sb	$Ag_nSb, n\approx3$
Arsenopyrite	Asy	$FeAsS$
Gudmundite	Gud	$FeSbS$
Non-sulphide Gangue	NSG	—
Intermediate Solid-Solution	iss	compositional phase-boundaries indicated in Fig. 12 (forthcoming)
Pseudo-Tetrahedrite	PT	stoichiometrically similar to Ttr
Bornite	Bor	Cu_5FeS_4
Partially Melted Galena	PGn	stoichiometrically similar to Gn
Approx. 95wt pct Ag-5wt pct Sb alloy	95Ag-5Sb	—

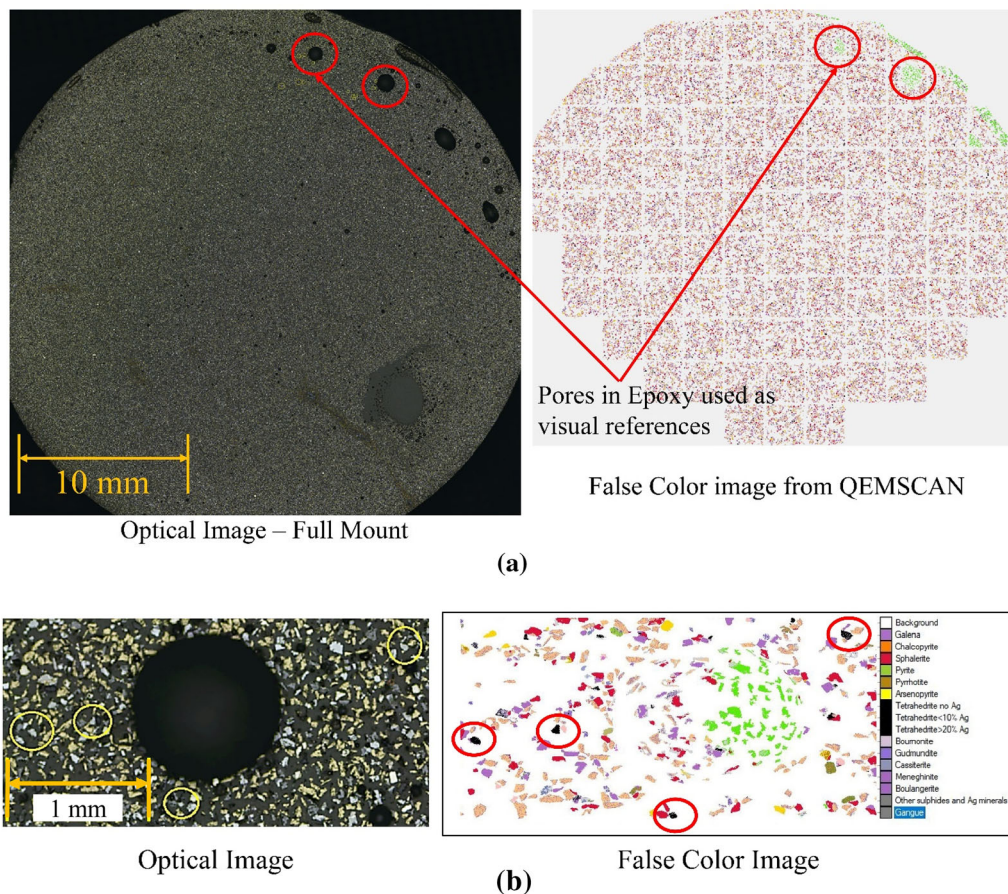| Property	Specification
Model	NWR193 Laser-Ablation System
Spot Geometry	circular
Spot Size, μm	25*, 10**
Laser Rate, Hz	10
Pulse Width, ns	< 4
Beam Profile	flat-topped, externally homogenized
ICP-MS Acquisition Dwell Time, s/cycle	0.375
Scan Speed, μm/s	8**
Maximum Return Speed, mm/s	5**

*Spot measurement.
**Element mapping.

Optical Image – Full Mount

False Color image from QEMSCAN

Pores in Epoxy used as visual references

(a)

Optical Image

False Color Image

(b)

Fig. 2—(*a*) Full-mount optical image (from optical microscope) and false-colored image (from QEMSCAN) of a 30mm diameter epoxy containing Garpenberg initial concentrate of 38 to 53 μm size fraction. The encircled pores in the epoxy were used as visual references for identifying the minerals to perform spot measurements in LA-ICP-MS (tetrahedrite bearing grains identified in the shown case); (*b*) Magnified optical and false-colored images around the pore which was marked with pointed arrows in (a). The identified tetrahedrite bearing grains are circled (Color figure online).

c. Non-quantification of LA-ICP-MS measurement data
The quantification of LA/ICP/MS cps/data into wt pct or ppm could not be satisfactorily accomplished. This could be related to certain known challenges in determining accurate element compositions from the LA-ICP-MS data for the sulphides, in addition to a few observations specific to this work listed below:

(1) *High compositional variability* Quantification of LA-ICP-MS data requires declaration of an element as an internal standard with its reliable and consistent wt pct content (predetermined). Certain minerals such as tetrahedrite investigated in this work exhibited considerable particle-to-particle variation in composition (details forthcoming in Sec-

tion III-B-1-b). An attempt of quantification was made for tetrahedrite using Cu as an internal standard, by determining its wt pct-content in different tetrahedrite grains through EDS-measurements. But, the results obtained were not satisfactory. For instance, the amount of some of the elements in the tetrahedrite though this quantification attempt came above 100 wt pct. Consequently, assignment of an appropriate internal standard for correct quantification was challenging.

(2) *Lack of versatile Standard Reference Material (SRM) for sulphides* Quantification necessitates standard reference materials (SRM) which are homogeneous, and physically and chemically similar to the unknown sample.[46] There are a few synthetic SRMs available in the sulphide matrix.[47–54] But these are generally customized to provide accurate quantification for specific samples. Besides, the natural sulphide minerals are unfit for usage as SRMs due to their inhomogeneity and lack of sufficiently wide range of trace elements. The well characterized SRMs in the silicate matrices such as the NIST 600 series are not suitable for the analysis of sulphide samples owing to matrix mismatch and certain chemical interferences.[48] Yuan *et al.*[55] proposed a method of using the silicate SRMs for the sulphides. It involved a calculation based on matrix normalization and sulphur internal standardization. Their method however endures an underlying assumption that there would be no difference of matrix effects between the silicate SRM and the sulphide mineral under investigation. Such an assumption would be rarely valid, considering the multiple effects such as high element-sensitivities and time-dependent inter-element fractionation in the sulphides compared to the silicates.[56] An attempt of quantifying the LA-ICP-MS data from tetrahedrite in the initial concentrate were made using MASS-1[47] as an SRM in this work. But, as mentioned earlier, the results were not satisfactory.

(3) *Problematic Sulphide behaviour during laser-ablation* There may be inaccuracies in the measured data due to the inherent material behavior of sulphides during laser-ablation. Sulphur transported in the vapour phase could interact with the material of the interface tubing connecting the laser-ablation cell and ICP-MS plasma unit, causing 'memory effects'.[57–62] Secondly, Gilbert *et al.*[38] reported melting of sulphide minerals during laser-ablation and the consequent element fractionation, with increasing severity in the below order for the tested minerals:

pyrite, sphalerite < pyrrhotite < pentlandite

< *c*halcopyrite < bornite < tetrahedrite

Evidently, the discrepancies related to the minerals such as tetrahedrite, bornite and chalcopyrite were found to be high. These minerals are of particular interest in the current investigation. Additionally, Figure 5 shows the BSE-image of a laser-ablation crater over a particle of tetrahedrite in the initial Garpenberg concentrate. Presence of separated phases with different BSE grey-levels in the ablated crater of originally tetrahedrite suggests the solidification of a melt phase. This is in line with the findings of Gilbert *et al.*[38] about the tendency of melting of tetrahedrite during laser-ablation.

(4) *Equipment limitations* Ultraviolet (UV) femtosecond laser-ablation pulse is found to result in accurate determination of element composition without any significant fractionation or matrix-effect in sulphide samples.[63,64] Similarly, laser beams with shorter wavelengths (such as 193 nm instead of the conventional 266 nm and 213 nm wavelengths) lead to a lower matrix effect.[38,46] The equipment used in the current research has a favorably low wavelength of 193 nm, but the pulse width duration is in nanometers (< 4 nm, Table III). Consequently, the issues of matrix-effects and element fractionation may still arise during the measurement over the sulphide minerals.

d. Statistical evaluation of LA-ICP-MS measurement data Considering the problems in quantification, the cps-signals from LA-ICP-MS after data-reduction were instead subjected to statistical evaluations.
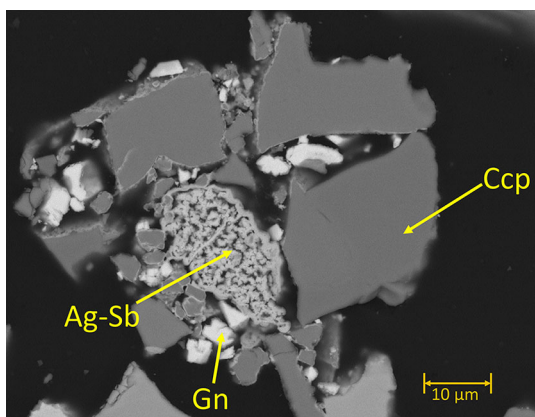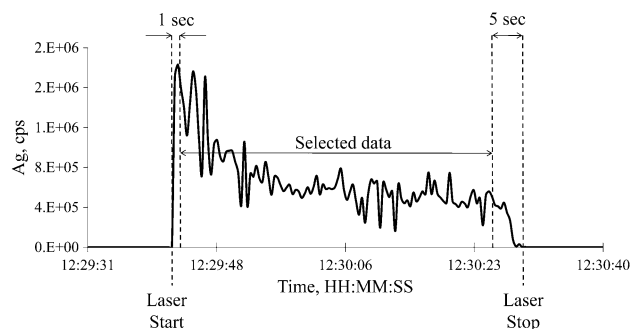

Fig. 3—Back Scattered Electron (BSE) image of a particle in the initial concentrate (38 to 53 μm) showing complex association of silver-antimonide phase with other minerals.

Fig. 4—Data reduction approach for the LA-ICP-MS spot measurements. The figure presents data (cps) for the channel ^{107}Ag at a spot of tetrahedrite in the Garpenberg initial concentrate. Data corresponding to the time interval between 1 s after the Laser-start till 5 s prior to the Laser-stop was selected for further processing.

The data of spot measurements performed over minerals in the initial concentrate was investigated using correlation matrices. For instance, in the case of tetrahedrite, all inter-element correlation coefficients between cps-signals for each spot were determined by generating a correlation matrix. Consistently high correlations over multiple spots between Sb (a major element in Ttr) and a specific trace element would suggest the presence of that trace element in the initial tetrahedrite. A similar such approach of evaluating occurrence relationships using inter-element correlation matrix was demonstrated by George et al.[29]

The cps-signals from the chemical mapping of melt-nugget microstructure were investigated through cluster analysis. Clustering of LA-ICP-MS data has been used previously for classification of elements in an assemblage of different phases.[40–43,65] In the current article, the clustering was performed using the cps-signals from mapping of the major and minor elements—Cu, Fe, Zn, Pb, S, Ag, Sb, As, S. Prior to the cluster-analysis, the cps/signals for each of these elements were suitably standardized (using the transformation expression, $(x - \sigma)/\mu$, σ = standard deviation, μ = mean). The algorithm of k-means clustering was used which divides the whole data-set into a specified number of clusters and allocates each data-point to one of those clusters. This clustering method is based on minimizing the Euclidean distance between the data-point and the mean of its assigned cluster. The clustering was executed using the Statistics and Machine Learning Toolbox of MATLAB 2020b (© 1994-2021 The Math-Works, Inc.). The aim of clustering was to replicate the different phases in the melt-nugget microstructure as these individual clusters. The intensities in cps of the trace elements in each of these clusters were subsequently analyzed for their classification in these phase-fractions in the melt-nugget.
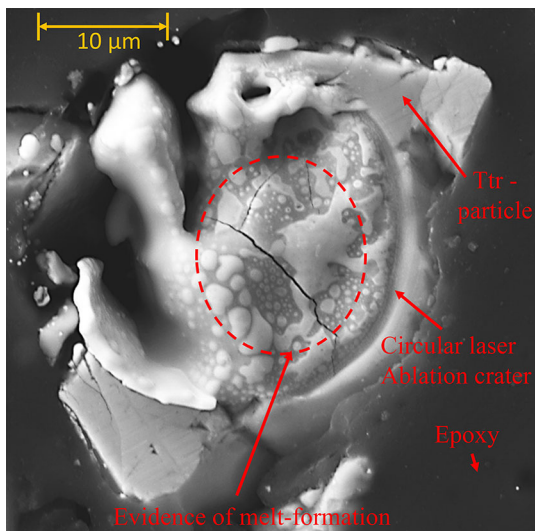

Fig. 5—BSE image of a circular laser-ablation crater (25 μm) over a particle of tetrahedrite in the initial Garpenberg concentrate (38 to 53 μm) showing evidence of a solidified melt.

III. RESULTS AND DISCUSSION

A. Characterization of Initial Concentrate for Minor (Ag) and Trace Elements

1. Ag-distribution in initial concentrate

The mineralogical composition of the initial Garpenberg concentrate obtained through QEMSCAN is presented in Figure 6(a). It was pointed out in an earlier study[22] that the proportion of tetrahedrite (Ttr) in the Garpenberg concentrate is significantly higher than that of the other sulfosalts—bournonite and meneghinite, also found in it. Ttr exhibited a wide variation in its Ag-content, whereas, Ag-Sb had specifically approx. 75 wt pct Ag, shown in the box-plot in Figure 6(b) of EDS-measurements. Figure 6(c) presents the Ag-intensities corresponding to the LA-ICP-MS spot measurements over various minerals in the initial concentrate. It suggests that Ag-Sb and Ttr are the main Ag-bearing minerals as their Ag-intensities are much higher than that of the other minerals. Tiu et al.[66] reported a minor Ag-content of 0.08 wt pct in galena (median value from EPMA analysis) at the Lappberget deposit belonging to the Garpenberg Mines.

The Ag-content in minerals other than Ag-Sb, Ttr and Gn were neglected. Subsequently, the Ag-distribution satisfying the 1.82 wt pct Ag-content (Table I) in the initial concentrate was calculated, as presented in Figure 6(d). Evidently, Ttr and Ag-Sb are the main Ag-carriers in the initial concentrate.

2. Trace elements distribution in initial concentrate

a. Identification of relevant trace elements Figure 7 illustrates the statistical method used in this work of determination of the significant trace elements present in minerals in the initial concentrate. Motivated from the concept of correlation matrix, element-pair-wise (for instance, Cu-vs-Co) values of correlation coefficients for each LA-ICP-MS spot measurement were collated into histograms to create a 'matrix of correlation-histograms'. In case of Figure 7, the inter-element correlation behavior is all-together presented for the 47 spot measurements of Ttr. Those histograms which have the frequency bars closer to the right side of the plot signify a strong correlation between the cps-signals of the corresponding element-pair. Additionally, a color-scheme is used for better visualization—leftmost bar in blue (poor correlation), rightmost bar in red (strong correlation), with smooth color-transition of bars along the x-axis.

The histogram-matrix in Figure 7 shows obvious strong correlations among the major elements in Ttr—Cu, Ag, Fe, Zn, Sb, As, S. To identify the prominent trace elements in Ttr, the histograms corresponding to Sb (a major element in Ttr) with the elements ϵ {Mn, Co, Ni, Ga, Se, Mo, Cd, In, Sn, Te, W, Au, Hg, Tl, Bi} were closely observed. All Sb-related correlation-histograms are in the row and column highlighted with broken lines in Figure 7. Relatively high correlations of Sb are found with Mn, Cd and Tl (marked with black-edged rectangles in Figure 7). Based on these correlation trends, it is
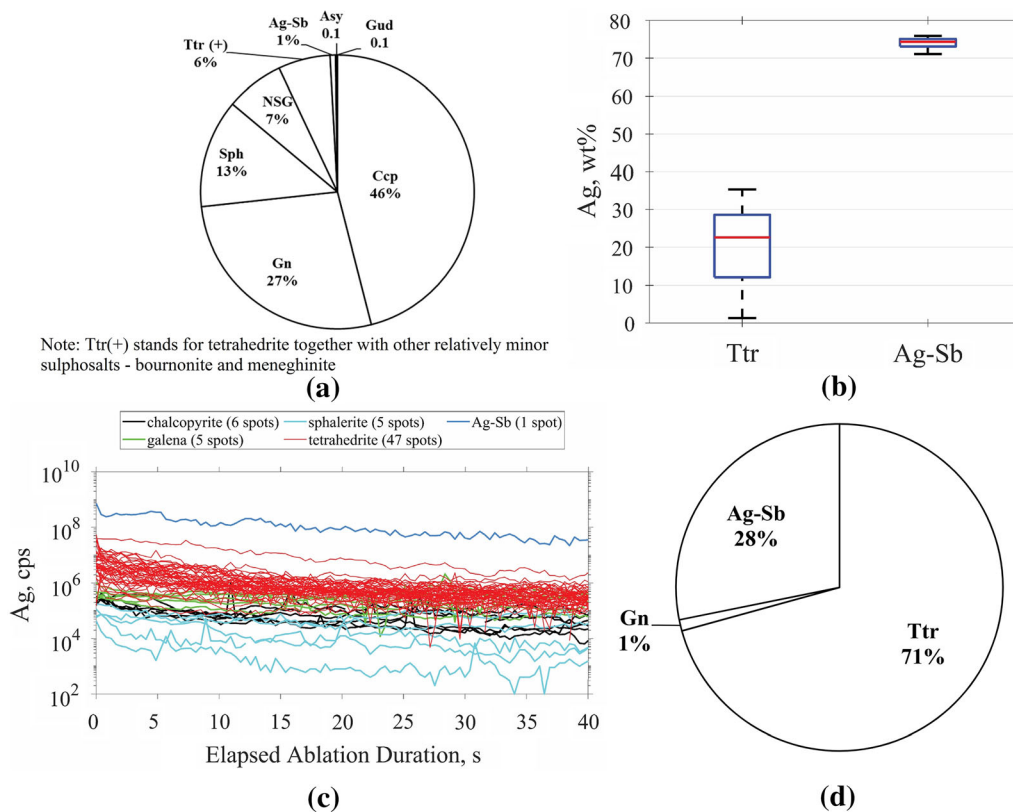
Note: Ttr(+) stands for tetrahedrite together with other relatively minor sulphosalts - bournonite and meneghinite

(a)

(b)

(c)

(d)

Fig. 6—(*a*) Mineralogical composition of Garpenberg Cu-rich Concentrate (initial concentrate) obtained from QEMSCAN; (*b*) Box plot of Ag, wt pct measurements from SEM-EDS on tetrahedrite (at 40 spots) and silver-antimonide (at 25 spots) in the initial concentrate; (*c*) Intensities in counts/s of LA-ICP-MS spot measurements (after data-reduction) in the initial concentrate; (*d*) Ag-distribution in the initial concentrate (determined by considering average Ag content in galena to be 0.08 wt pct [66] and Ag-content in the initial tetrahedrite as 22.6wt pct based on the median value in the boxplot (b).

therefore estimated that Mn, Cd and Tl are present in trace concentrations in Ttr in the initial Garpenberg concentrate.

Notably, Sb additionally shows sufficiently good correlations with Pb in Figure 7. This can be related to the known close-association between Gn and various Ag-rich phases in the Garpenberg deposit, reported by Sandecki *et al*.[67] Gn and Ttr were found to frequently co-exist, one occurring often in the matrix of another as micro-inclusion. The presence of Gn micro-inclusions in Ttr would justify such trends of good correlations between Sb-*vs*-Pb in the data of LA-ICP-MS spot measurement over Ttr.

Similar inter-element correlation-histograms are presented in Figure 8 for the other minerals—Ccp (6 spots), Sph (5 spots), Ag-Sb (1 spot) and Gn (5 spots). For identification of relevant trace elements, the correlation-histograms corresponding to Cu for Ccp, Zn for Sph, Ag for Ag-Sb and Pb for Gn were particularly analysed. Ccp did not exhibit prominence of any trace

element. Whereas, the other histogram matrices in Figure 8 demonstrated that Sph has Mn, Cd, Hg; Ag-Sb has Cd, Hg; and, Gn has Tl in trace concentrations.

b. Determination of principal mineral-hosts for trace elements Figure 9 presents the cps-signals of the identified relevant trace elements—Tl, Mn, Cd and Hg for various minerals in the initial Garpenberg concentrate. It shows that Tl is relatively much higher in Gn compared to the other sulphide minerals. Similarly, Sph is the main carrier for Mn, Cd and Hg. Cd is present in comparable concentrations in Ttr and Sph.

It may be noted that Sph is the principal host of trace elements amongst various minerals in the initial concentrate. This is in line with the previous studies which highlighted the role of crystal structure of Sph (composed of FCC lattice with tetrahedrally coordinated Zn and S) in facilitating accommodation of a wide range of trace elements.[26,68–70] The crystal structure of Ttr is
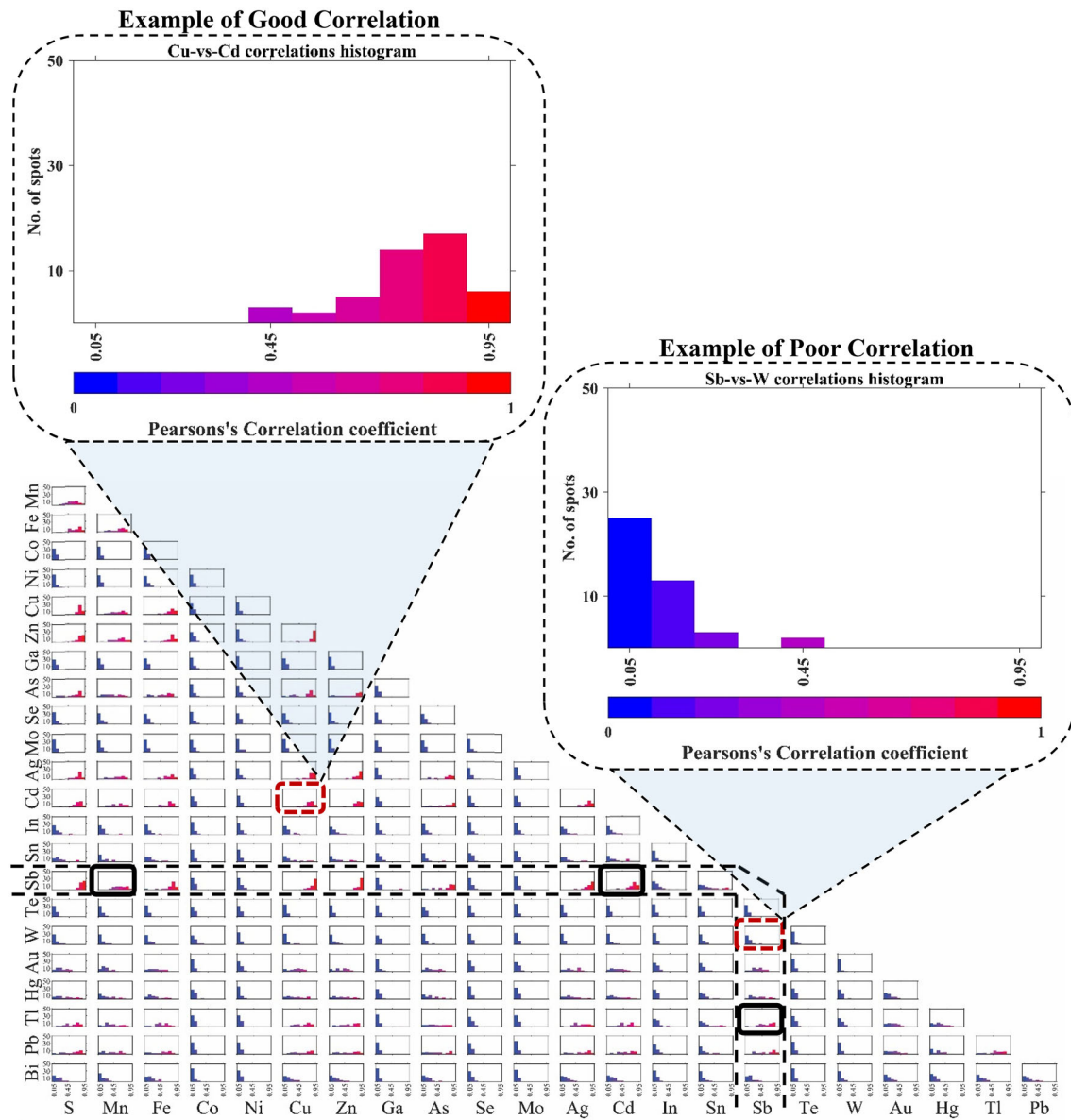
Fig. 7—A matrix of histograms for correlation coefficients between the intensities (cps) of all pairs of measured isotopes in LA-ICP-MS for the initial tetrahedrite. Each histogram is built using the data of spot measurements at 47 sites (after data-reduction) of tetrahedrite. Y-axis of each histogram represents the number of spots belonging to each bin (sub-interval) of Pearson's correlation coefficient values for the respective isotope pairs. Consequently, sum of all the bar heights in each histogram is 47. Bin-width for the correlation coefficient values along x-axis is 0.1. A color scale is used to fill varying colors in the different bars of the histogram along x-axis (for better visualization and interpretation of the correlation data, blue-'poor correlation', red—'good correlation'). Two histograms from the matrix are magnified, one showing good correlations between the selected pair (bars mostly nearer to the right edge of the x-axis), and another showing poor correlations (bars mostly nearer to the left edge of the x-axis). The row and column in the matrix corresponding to the correlation of Sb (main element in tetrahedrite) with other elements are highlighted using broken lines. Sb has strong correlations with the trace elements Mn, Cd and Tl from the list ϵ {Mn, Co, Ni, Ga, Se, Mo, Cd, In, Sn, Te, W, Au, Hg, Tl, Bi}, again highlighted using rectangular boxes with black edges (Color figure online).

considered as a derivative of the atomic arrangements in Sph.[71,72] Such an attribute could account for the similar intensities of one of the relevant trace elements—Cd in Sph and Ttr.

Regarding the relatively high intensities of Tl corresponding to spot measurements over Gn in Figure 9, Cook et al.[25] also reported correlation between Tl and Pb in their LA-ICP-MS measurements over bornite.

They attributed the coherent and flat time-resolved Tl- and Pb-profiles in laser data to the occurrence of homogeneously distributed Pb-Tl sulphosalts. In the current investigation, Figure 9 suggests that galena is likely the major host of Tl in the initial Garpenberg concentrate. However, determination of the actual Tl-bearing phase in galena is out of scope of this work.
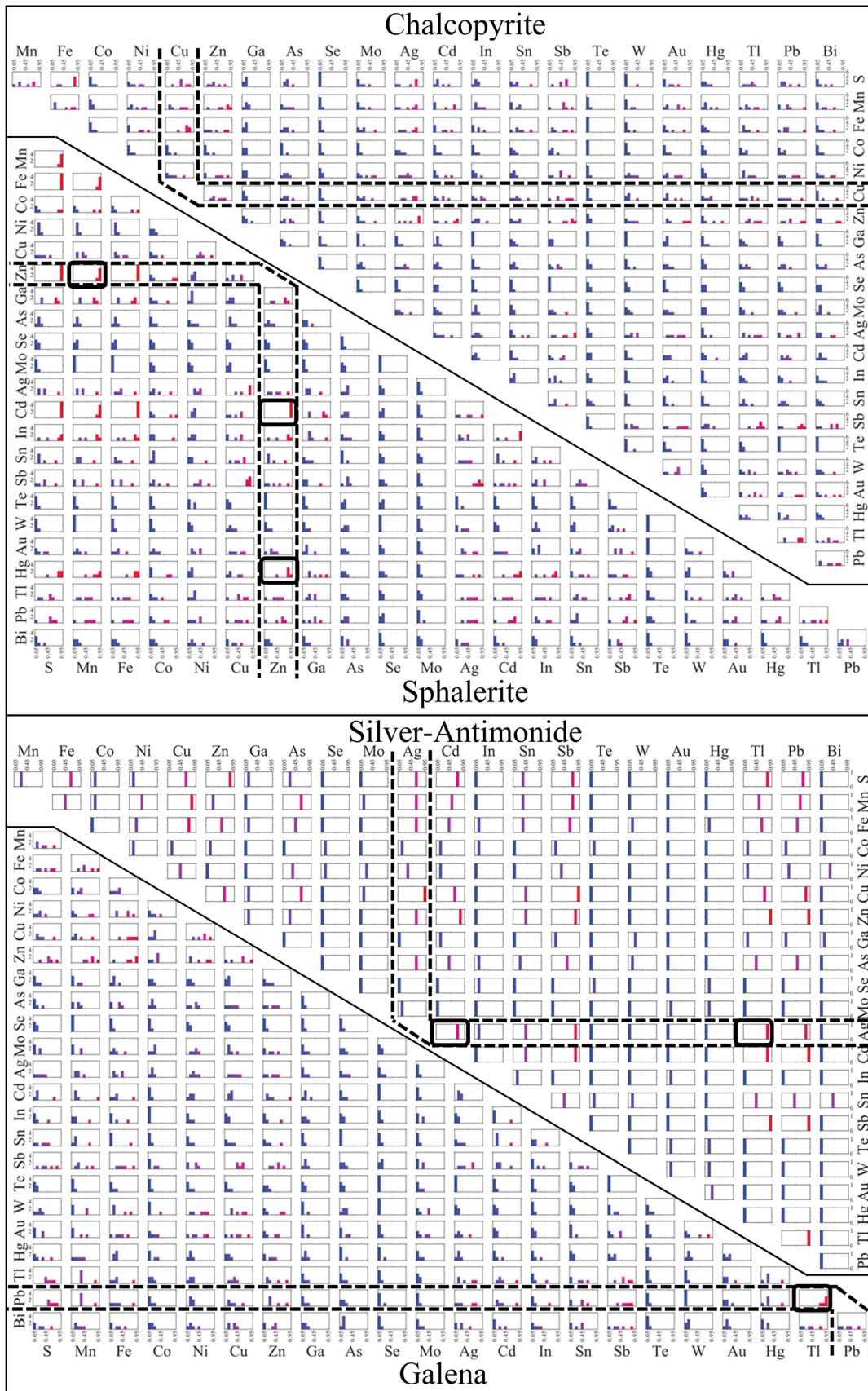
◄ Fig. 8—Inter-element matrices of correlation-histograms for the LA-ICP-MS spot measurements over chalcopyrite (6 spots), sphalerite (5 spots), silver-antimonide (1 spot) and galena (5 spots) in the initial Garpenberg concentrate. The bar-coloring-scheme along the x-axis is same as that followed in Fig. 7. The row and column in each of these matrices for the main element corresponding to each mineral are highlighted using broken lines. -Cu for chalcopyrite, Zn for sphalerite, Ag for silver-antimonide and Pb for galena. The trace elements ϵ {Mn, Co, Ni, Ga, Se, Mo, Cd, In, Sn, Te, W, Au, Hg, Tl, Bi} showing strong correlations with the main element in each mineral are highlighted using black-edged rectangular boxes (Color figure online).

B. Characterization of melt-nugget for minor (Ag) and trace elements

1. Evaluation of major phase transformations during roasting

Figure 10(a) presents the optical image of microstructure of a melt-nugget in the roasted calcine. Since the melt nuggets were entrapped in the sintered calcine [Figure 1(b)], they would have formed through trickling and accumulation of liquids at the roasting temperature. The microstructure in Figure 10(a) would therefore essentially constitute the phases which were liquid at 700 °C. The chemical maps for this microstructure obtained from SEM-EDS are shown in Figure 10(b) through (g). The maps for Fe [Figure 10(c)] and Zn [Figure 10(e)] are reasonably similar. The other four maps are quite distinct, suggesting that there are 5 phase-fractions in the melt nugget—Cu-rich, Sb-rich, (Zn,Fe)-rich, Pb-rich and Ag-rich. Table IV lists the details of these phase-fractions obtained from SEM-EDS.

The melt phase-fractions and associated transformations in this sample were partly described in our previous work in Prasad et al.[21]. Liquid formation was mainly associated with partial melting of galena (PGn) to form two low-melting liquids which subsequently solidified as coarse (iss-PGn) and fine (PT-PGn) intergrowths. These two different forms of intergrowths can be seen in the microstructure in Figure 10(a). 'Partial melting' of galena is assumed owing to the heterogeneous nature of the concentrate as a mineral-mixture. Melting of only those galena-bearing particles would take place which were in physical contact with the particles bearing iss and/or tetrahedrite. The thermodynamic basis for the partial melting of galena resulting in such intergrowth patterns in the microstructure are:

(1) Existence of a low-melting eutectic on the PbS-Cu_3SbS_3 join in the Cu_2S-PbS-Sb_2S_3 ternary system.[14,15,21,60]

(2) Evaluations of the Cu-Fe-Pb-S system by Craig et al.[73] and Stevens et al.[16] suggesting that a melt formation on the $CuFeS_2$-PbS join would occur between 630 °C and 700 °C.

Apart from iss, PT and PGn, there are two additional phase-fractions—Bor and 95Ag-5Sb in the microstructure in Figure 10(a), which shall be elaborated in this article. Notably, the rounded (i.e. lacking sharp boundaries) and irregular patterns of the constituent phase-fractions in the microstructure in Figure 10(a) suggest that there were multiple immiscible liquids at the roasting temperature.[74,75] Multiple immiscible liquids comprising of sulphides, Sb-As-sulphosalts and sulphur-devoid metallic alloys have also been reported in earlier investigations on metamorphism in complex polymetallic sulphide deposits.[15,76,77] A thermodynamic explanation for such extensive liquid immiscibilities has been based on the concept of thermal divide. For instance, the PbS-$CuSbS_2$ and PbS-$AgSbS_2$ joins act as thermal divides between sulphide and sulphosalt melts in Cu_2S-PbS-Sb_2S_3[14] and Ag_2S-PbS-Sb_2S_3[78] ternary systems, respectively. Veksler et al[79] have elaborated a configuration in which a thermal divide beneath a liquid-immiscibility dome would result in multiple crystallization sequences. Solidification from within the immiscibility dome would progress with liquids enriching in different direction inside the phase diagram, owing to the occurrence of a thermal divide between multiple eutectics. Interestingly, $CuSbS_2$ and $AgSbS_2$ have melting points of 556.2°C[80] and 510°C,[81] respectively, which are below the experimental temperature of 700°C presented in this work. The PbS-$CuSbS_2$ and PbS-$AgSbS_2$ joins could therefore offer such configurations in which the immiscible liquids would encounter an underneath thermal divide during the sequence of solidification.

a. Precipitation of Bornite Figure 11 presents the elemental composition data obtained through SEM-EDS for the phase pointed by 'Arrow 3' in Figure 10(a). Evidently, this phase is chemically close to bornite, Cu_5FeS_4 (theoretical composition - 50 mol. pct Cu, 10 mol. pct Fe and 40 mol. pct S).

Considering the CuS-FeS-ZnS ternary phase diagram shown in Figure 12, there exists an extensive solid-solution phase—iss[12] at 700°C. Consequently, the initial Ccp transforms to iss-phase at high temperature through solid-state assimilation of co-existing Fe- and Zn-bearing minerals, as elaborated previously in Prasad et al.[21]. The extent of additional Fe and Zn going in the initial Ccp is dictated by—(1) the overall elemental composition of the initial concentrate (i.e. Fe wt. pct beyond what is existing as Ccp, and Zn wt pct in the initial concentrate), (2) the compositional limit of the iss-phase set by its isotherm at 700°C shown in Figure 12. Now, based on the chemical composition of the initial Garpenberg concentrate presented in Table I, the point in the phase diagram representing the assimilation by initial Ccp of all available Fe and Zn in the initial concentrate is calculated and marked by a red-square in Figure 12. It is expected that the transformation of Ccp to iss-phase would follow the compositional change in the direction of the indicated arrow. This arrow is along the line joining the position of CuS:FeS = 50:50 (initial composition of Ccp, marked by point A) and the calculated Fe + Zn + Ccp position shown by the red-square (point B). The expected linearity in composition change along the line AB during the iss-phase evolution is due to the fact that there are essentially two minerals participating in the iss-phase evolution—Ccp and Sph.
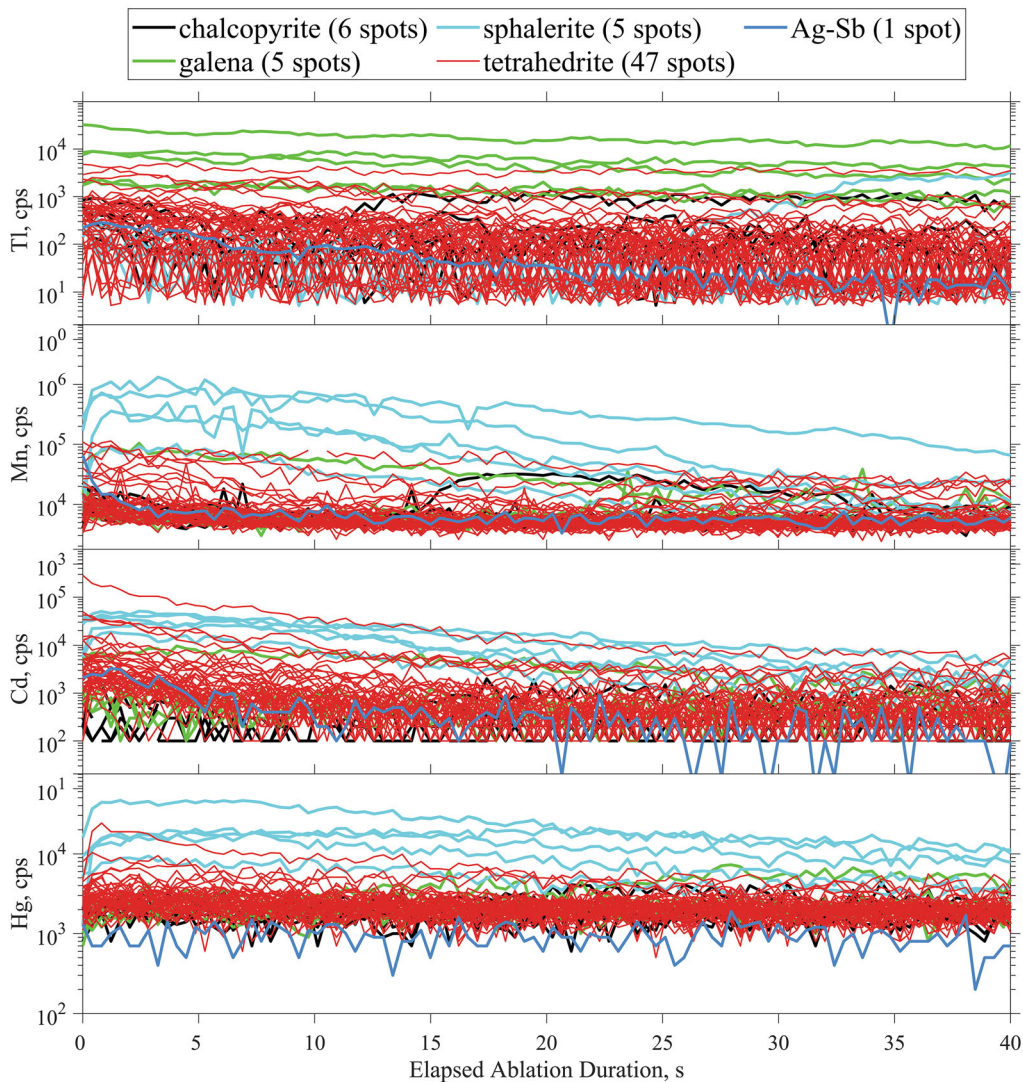
Fig. 9—LA-ICP-MS spot measurement intensities in counts/s for the prominent trace elements—Tl, Mn, Cd, Hg in the various minerals in the initial Garpenberg concentrate.

The Fe-rich Py mineral could not be detected in this concentrate during the QEMSCAN [Figure 6(a)] and XRD[21] measurements. The compositional change would however be restricted till point C on the 700 °C-isotherm, as the red-square lies outside the iss-phase field. Point B and C are at similar Fe-levels, but the difference is significantly high in ZnS (mol. pct) between these two points. Consequently, if the compositional change stops at point C, there will be a significant amount of surplus-Zn available in the mineral assemblage, un-assimilated in the iss-phase. The actual composition of the iss-phase in the melt microstructure measured by SEM-EDS are also overlaid in Figure 12, which are mostly located near point D on the isotherm. Notably, the points—D and B are at similar Zn-levels. The final iss-composition at 700 °C being around point D instead of point C means there has been an expulsion of certain amount of Cu from the iss-phase to gain the surplus-Zn from the mineral

assemblage. This would explain the occurrence of bornite (the Cu-rich phase-fraction) in the melt-nugget microstructure in Figure 10(a). It is likely that the Bor precipitated out to facilitate the total assimilation of Sph in the iss-phase at 700 °C.

In a strictly Cu-Fe-S system, Bor and iss-phase are known to form a low-melting eutectic below 800 °C.[82,83] Inclusion of additional elements such as Zn, Pb, Ag, Sb, As (as in the presently investigated system of the Garpenberg concentrate) would likely reduce the melting point of this eutectic-phase combination further down. Interestingly, Bor exists primarily in the gaps between the solidified intergrowth phases in the microstructure in Figure 10(a). The thermodynamic phase-relations of Bor with the co-existing phase-fractions (such as with iss) together with its microstructural attribute suggest that Bor was supposedly the last liquid to solidify during cooling of the roasted calcine.
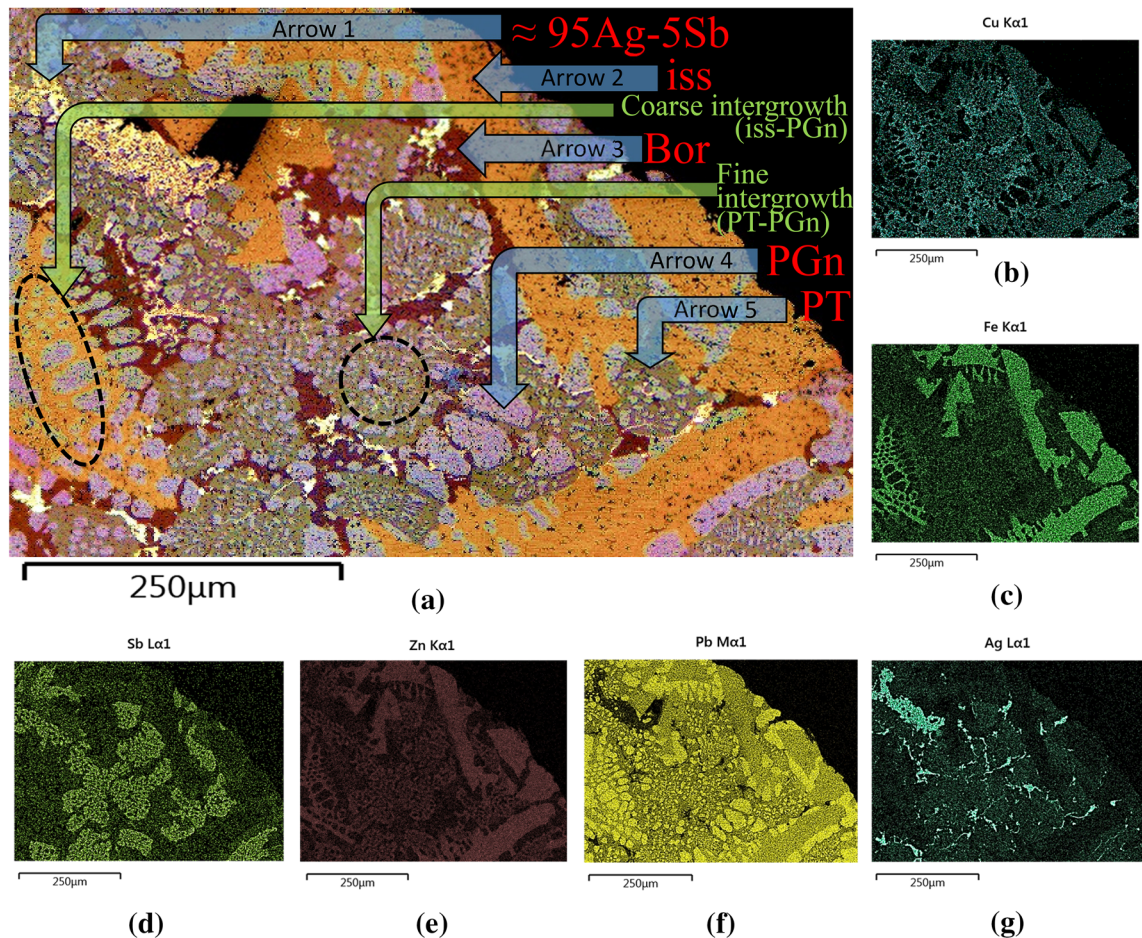
Fig. 10—(*a*) Optical microscopic image of a melt nugget (macroscopic view in Fig. 1(b)), in which the identified phases have been indicated. (*b*) to (*g*) Element mapping of the microstructural area, obtained from SEM-EDS. The elemental mapping images suggest that the bright-yellow colored phase in (a) pointed by 'Arrow 1' is Ag-rich. Similarly, the orange colored phase pointed by 'Arrow 2' is Fe-rich, the dark-brown-colored phase pointed by 'Arrow 3' is Cu-rich, the light-purple colored phase pointed by 'Arrow 4' is Pb-rich, and, the greenish phase pointed by 'Arrow 5' is Sb-rich (Color figure online).

b. Ag-separation from tetrahedrite to form 95Ag-5Sb alloy In addition to the iss-PGn, PT-PGn intergrowths and Bor-phase-fraction, the microstructure in Figure 10(a) also comprises of a bright-yellow phase-fraction which is Ag-rich [Figure 10(g)]. EDS-measurements over this phase revealed that its composition is approximately 95Ag-5Sb (wt pct), which is presented in Figure 13(a) along with the EDS-measurements corresponding to the Ag-Sb mineral phase in the initial concentrate. Clearly, the newly formed phase is richer in Ag compared to the initial Ag-Sb (comprising approx. 75 wt pct Ag). Apparently, there has been mobilization of Ag from other mineral phases to join the Ag-Sb phase during roasting. Since Ttr and Ag-Sb were the principal Ag-carriers in the initial concentrate [Figure 6(d)], this significant Ag-enrichment in Ag-Sb phase during roasting would signify transfer of Ag from Ttr into Ag-Sb.

Ag is known to substitute up to 6 Cu atoms at the monovalent sites in a formula unit of $Cu_{12}Sb_4S_{13}$ (theoretical tetrahedrite). Also, in most of the natural tetrahedrites, Cu occupies a maximum of up to 10 (6 Cu^+, 4 Cu^{2+}) of its designated 12 sites. The balance 2 divalent sites are generally occupied by Fe^{2+} and Zn^{2+}.[84] Such Cu-Ag compositional attributes can be seen in Figure 13(b) obtained from EDS measurements over Ttr in the initial Garpenberg concentrate. Ttr exhibits wide-compositional variation with a linear relationship between Cu and Ag. There is evidently a full-range of solid-solution in Ttr constituted by two end members—(1) Ttr containing 6 Ag atoms p.f.u. (per formula unit), and (2) Ttr containing 10 Cu atoms p.f.u. During roasting, Ttr transforms into pseudo-tetrahedrite (PT) in the process of forming a low-melting eutectic with Gn.[19–21] It can be observed from Figure 13(b) that this Ttr→PT transformation resulted in loss of Ag from the initial Ttr. The PT melt phase-fraction has a relatively very low Ag-content, implying release of Ag from Ttr at high temperature. Supposedly, the Ag-Sb mineral phase was joined by the Ag released from Ttr resulting in the formation of 95Ag-5Sb melt phase-fraction.

2. Classification of trace elements based on cluster analysis of LA-ICP-MS mapping data

a. Cluster evaluation and validation Figure 14(a) presents an SEM image of the microstructural site in the melt-nugget which was characterized by LA-ICP-MS for chemical mapping. The rectangular area which was mapped is highlighted, showing the rows of laser-ablation craters. The thickness of these rows is 10 μm, which is the selected spot-size for chemical mapping. Figure 14(b) is the optical image of the same microstructural site, acquired prior to the laser-ablation. The rectangular area in this microstructure undergoing subsequent laser-ablation is again highlighted in this image.

The generated dataset of cps-signals from the LA-ICP-MS chemical mapping for the major and minor elements ϵ {Cu, Pb, Zn, Ag, As, Sb, S} was appropriately standardized. The standardized dataset was repeatedly subjected to k-means clustering analysis for 8 times, only changing the pre-assigned number of data-clusters from 1 to 8 over these runs. Figure 14(c) presents the plot of summation for within-cluster point-to-centroid Euclidean distance obtained in each run. The summation distance is found to reduce significantly until 5

clusters, beyond which the decrease is relatively small. It is suggestive of the existence of optimal 5 clusters in the standardized chemical-mapping dataset. This is consistent with the existence of 5 phase-fractions in the melt-nugget microstructure—iss, PT, PGn, Bor and 95Ag-5Sb. To further validate the clustering approach, a false-colored rastered image was produced based on the cluster numbers ϵ {1, 2, 3, 4, 5} assigned to each measurement data-point. This image presented in Figure 14(d) closely resembles the phase assemblage in the rectangular area in Figure 14(b). For instance, portions in Figure 14(d) representing Cluster 1 in white-color match consistently with the light-purple colored PGn phase-fraction in the original microstructure in Figure 14(b). [The light-purple colored phase in the melt-nugget microstructure was identified as PGn earlier in Figure 10(a)]. Such an effective reproduction of microstructure of the laser-ablated area implies that each data-cluster corresponds to one of the 5 phase-fractions in the melt-nugget microstructure.

b. Trace elements classification Since the 5 identified melt phase-fractions were distinctly rich in one of the elements ϵ {Cu, Fe, Pb, Sb, Ag}, the cps-signal intensities for these elements in the LA-ICP-MS chemical-mapping dataset were compared between the 5 data-clusters. These comparisons are shown in Figure 15(a) through (e).

Evidently, Cluster 1 is Pb-rich and thereby represents PGn melt phase-fraction. Similarly, Cluster 2 being Cu-rich represents Bor; Cluster 3 being Fe-rich represents iss; Cluster 4 being Sb-rich represents PT; and, Cluster 5 being Ag-rich represents 95Ag-5Sb. These relationships between data-clusters and melt phase-fractions are also in line with the matching of clusters in the reproduced microstructure in Figure 14(d) with the phase-fractions in the original microstructure in Figure 14(b). However, it is important to note that the order-of-magnitude comparison of cps-signals for these elements {Cu, Fe, Pb, Sb, Ag} between different clusters/phase-fractions in Figure 15 is not valid in this study. The spot size of 10 μm for the LA_ICP-MS chemical mapping would not be sufficiently small enough to consistently represent only a single phase-fraction. Especially, in the regions of finer intergrowths in Figure 14, the ablated material from each spot in the rastered-scan would be a mixture of multiple phase-fractions. However, as pointed out earlier in Section III-B-2-a, the clustering method could
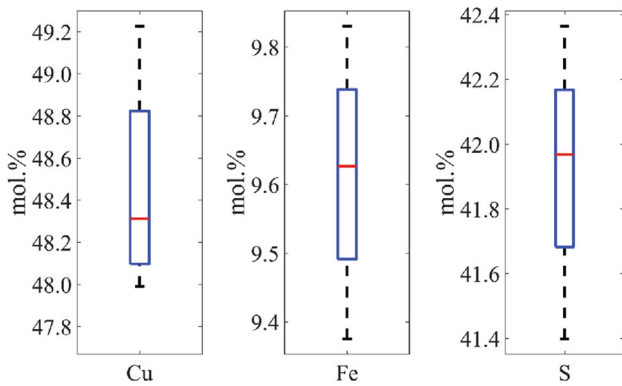

Fig. 11—Box plot of Cu, Fe and S contents (mol. pct) from the EDS spot measurements at the Cu-rich sites (dark-brown-colored phase in the melt microstructure marked by 'Arrow 3' in Fig. 10(a)), suggesting its resemblance in stoichiometry with Bornite (Cu_5FeS_4). In this box plot, the bottom-edge of the rectangle corresponds to the 25th percentile (Q1) of the multiple EDS measurements. Similarly, the top-edge corresponds to the 75th percentile (Q3). The red line inside the rectangle represents the sample median. The vertical edge-length of the rectangle is the inter-quartile range (IQR). The error bar corresponds to the extreme values which are within [Q1 − 1.5 × IQR Q3 + 1.5 × IQR] (Color figure online).

Table IV. Details of Phase-Fractions in the Microstructure of Melt-Nugget, Presented in Fig. 10(a)

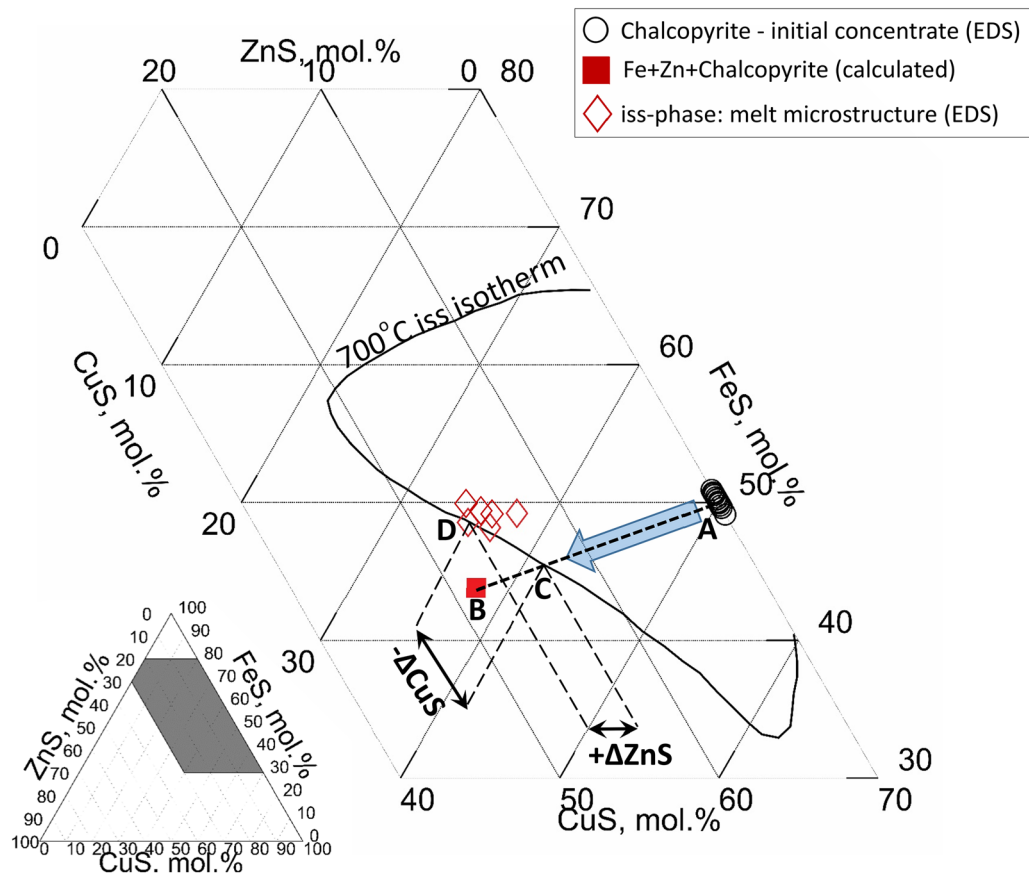| Sl. No.	Microstructural Appearance in Fig. 10(a)	Identified Phase	Reference for EDS-Measurement Data
1	Bright-yellow, pointed by Arrow 1	95Ag-5Sb	Fig. 13(a)
2	Orange, pointed by Arrow 2	iss	Fig. 12
3	Dark-brown, pointed by Arrow 3	Bor	Fig. 11
4	Light-purple, pointed by Arrow 4	PGn	Prasad *et al.* [21]
5	Green, pointed by Arrow 5	PT	Prasad *et al.* [21]

Fig. 12—A portion of CuS-FeS-ZnS ternary diagram (inset in left bottom corner) showing the 700oC isotherm of iss-phase obtained from Kojima *et al.* [12] (adapted with permission from Kojima *et al.* [12]).The EDS-measured compositions of *chalcopyrite* in the initial concentrate (marked by open-circles), and of iss-phase (marked by 'open diamonds') in the melt-nugget microstructure are included in the ternary plot. The measured compositions of initial chalcopyrite are very close to the theoretical composition of CuS:FeS = 50:50. A calculated composition assuming that the initial chalcopyrite assimilates all the available Fe and Zn from other minerals during roasting at 700oC is plotted as 'red colored square' (Color figure online).

overcome this problem of phase-mixing and could effectively classify the measured spots into representative clusters.

The relevant trace elements identified earlier in Section III-A-2-a were—Tl, Mn, Cd and Hg. The cluster-wise comparison of their cps-signals (from LA-ICP-MS chemical mapping) are presented in Figure 15 (f) through (i). It can be noticed in Figure 15(f) through (g) that the intensities for Tl and Mn are relatively high for Cluster 2 (Bor). It suggests that Tl and Mn segregated in the Bor-phase-fraction during solidification of the melt. Similarly, Cd-intensities being high for Cluster 4 (PT) in Figure 15(h) would indicate the segregation of Cd in the PT phase-fraction. Notably, Hg-intensities are in similar ranges for all clusters [Figure 15(i)]. Apparently, Hg was homogeneously distributed in all the phase-fractions, and did not undergo any noticeable segregation during solidification.

The preferential redistribution of individual trace elements into selective melt phase-fractions could be associated with numerous factors. Minerals such as Ttr and Bor occur naturally as complex superstructures which can accommodate trace elements through solid-solutions, inclusions or structural defects.[25,71,85] Concurrently, the order of solidification of multiple liquids could be relevant, as many trace elements could partition into the low-melting phases. For instance, the microstructural attribute of Bor in Figures 10 and 14 as a phase filling the gaps between intergrowth phases points towards its subsequence in the solidification-order. However, detailed explanation of the phase-preferences of individual trace elements during melt-nugget solidification necessitates further research, which is not in the scope of the present study.

C. *Minor (Ag) and Trace Elements Re-distribution Summary*

Table V summarizes the findings from the various investigations presented in this work regarding the initial occurrence of the minor and trace elements, and their subsequent migration due to roasting of the Cu-rich Garpenberg concentrate.

Evidently, Bor which apparently was the last liquid to solidify acted as a sink to accumulate quite a few trace elements (Mn, Tl) during solidification. Such a demonstration of concentrating trace elements (originally present
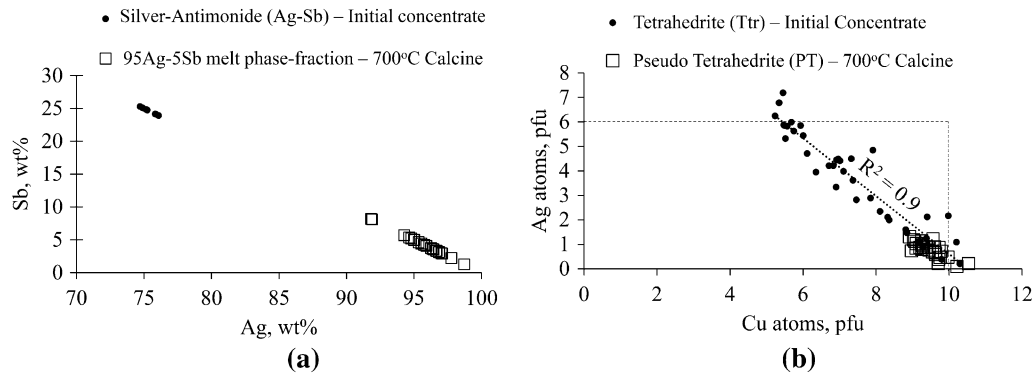
Fig. 13—(*a*) Composition of Ag-Sb phase in the initial concentrate and the Ag-rich phase-fraction (bright-yellow colored phase indicated by Arrow 1 in Fig. 10(a)) in the melt-nugget of the roasted calcine, suggesting enrichment of Ag in the initial Ag-Sb mineral during high temperature treatment to reach a composition of nearly 95Ag-5Sb(wt pct) (*b*).
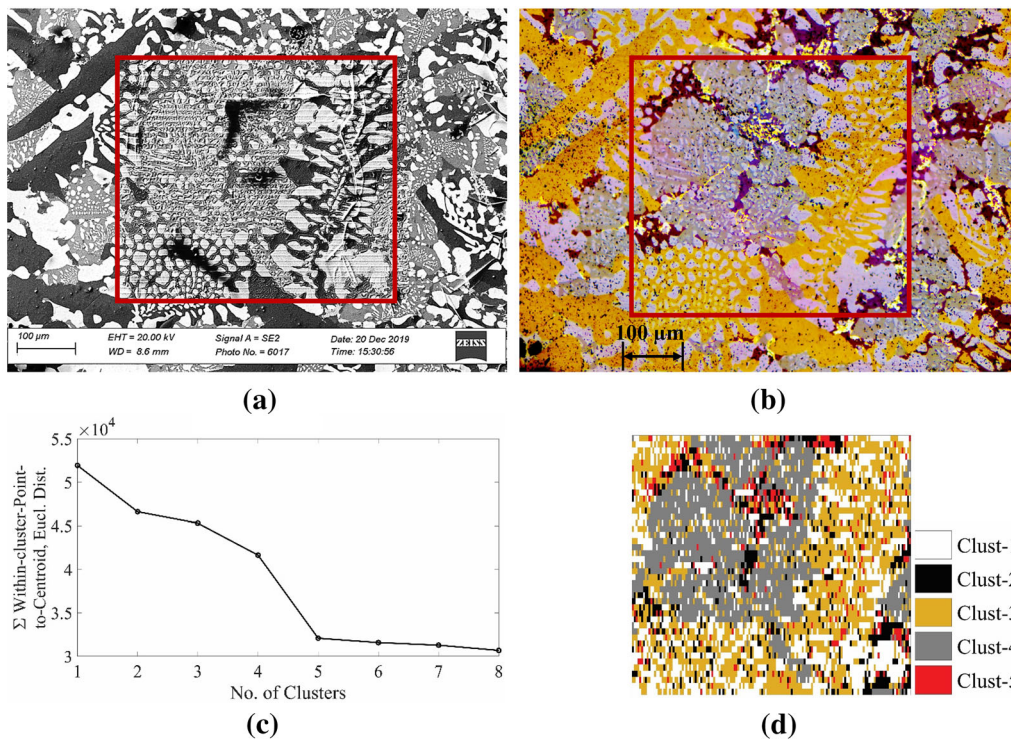

Fig. 14—(*a*) Secondary Electron (SE) image of a microstructural site in the melt nugget (this site is different from that shown in Fig. 10(a)), depicting the rows of laser-ablation craters (performed for chemical mapping) within the red-colored rectangular area (*b*) Optical image of the same microstructural site (before laser ablation), also highlighting the area analyzed for chemical mapping. (*c*) Sum of point-to-centroid Euclidean distances—*vs*—number of clusters, obtained from 'k-means' cluster analysis of the cps-data (for Cu, Pb, Zn, Ag, As, Sb, S) from LA-ICP-MS chemical mapping. The optimum number of clusters found in the dataset is 5. (*d*) Reproduced microstructure of the mapped area highlighted in (a) and (b), obtained by considering 5 clusters (Color figure online).

in different minerals) into a few low-melting phase-fractions could insinuate new strategies for extraction of trace elements from sulphide mineral assemblies. Notably, the surplus availability of Sph in the initial Garpenberg concentrate (beyond the limits set by the 700 °C-isotherm of the iss-phase for Zn-assimilation into Ccp) led to precipitation of Bor, which eventually exhibited this tendency of trapping trace elements during solidification.

IV. CONCLUSIONS

Following conclusions could be drawn based on evaluation of the phase transformations in the Cu-rich Garpenberg concentrate (polymetallic complex sulphide concentrate) due to roasting in Nitrogen atmosphere at 700 °C:
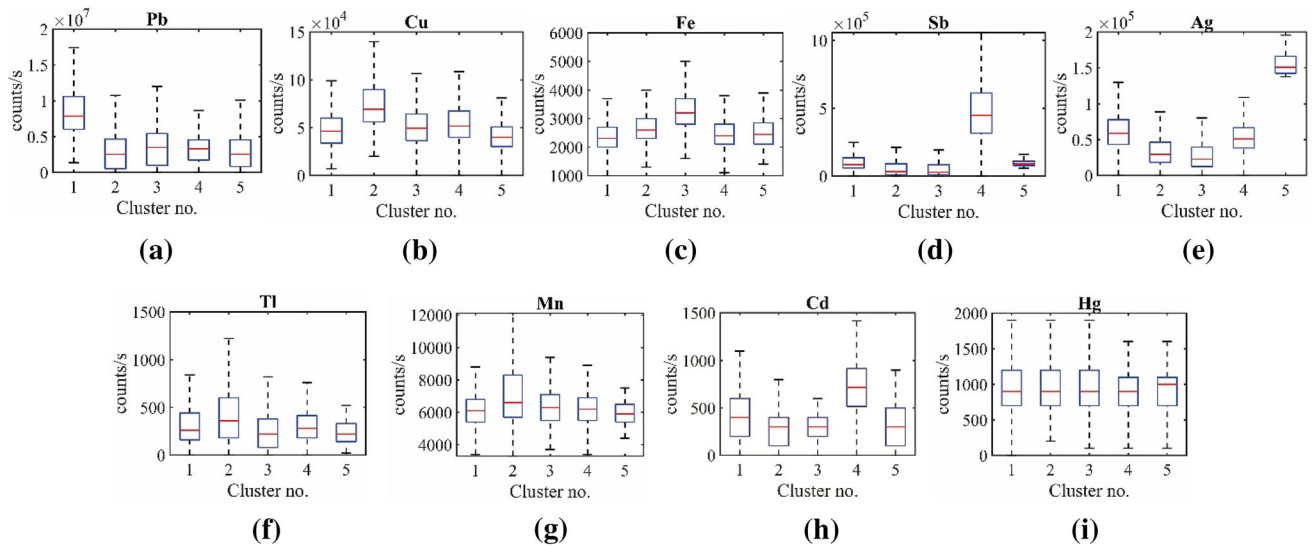
Fig. 15—Box-plots for the major elements—(*a*) Pb, (*b*) Cu, (*c*) Fe, (*d*) Sb; minor element—(*e*) Ag; and the trace elements—(*f*) Tl, (*g*) Mn, (*h*) Cd, (*i*) Hg w.r.t the different clusters obtained from 'k-means' cluster analysis of the cps-data (for Cu,Pb,Zn,Ag,As,Sb,S) from LA-ICP-MS chemical mapping. (a) suggests that Cluster 1 belongs to the PGn phase due to its highest Pb intensity range. Similarly, Cluster 2 belongs to Cu-rich Bor, Cluster 3 belongs to Fe-rich iss, Cluster 4 belongs to Sb-rich PT, and Cluster 5 belongs to Ag-rich 95Ag-5Sb(wt pct) melt phase-fraction. (f) and (g) suggest that the trace elements Tl and Mn segregated in Bor (Cluster 2), whereas Cd segregated into the PT (Cluster 4) melt fraction. Hg was found to disperse homogeneously in all the melt phase.

Table V. Summary of Redistribution of Minor and Trace Elements During Roasting of Cu-Rich Garpbenberg Concentrate at 700°C in N$_2$ Atmosphere

Type	Element	Before roasting primary hosting mineral	After roasting primary hosting melt phase-fraction
Minor	Ag	tetrahedrite (Ttr), silver-antimonide (Ag-Sb)	95Ag-5Sb
Trace	Cd	sphalerite (Sph), tetrahedrite (Ttr)	pseudo-tetrahedrite (PT)
	Mn	sphalerite (Sph)	bornite (Bor)
	Hg	sphalerite (Sph)	evenly distributed
	Tl	galena (Gn)	bornite (Bor)

(1) There exists a wide-ranged tetrahedrite solid-solution in the Cu-rich Garpenberg concentrate. This is evident from the extensive Cu-vs-Ag composition variability in the tetrahedrite-bearing particles. The compositions of tetrahedrite uniformly vary across the two end members—(I) Tetrahedrite consisting 6 Ag atoms p.f.u (per formula unit), (II) Tetrahedrite consisting of 10 Cu atoms p.f.u.

(2) Tetrahedrite and silver-antimonide are the principal Ag-carriers in the Garpenberg concentrate.

(3) Roasting at 700°C in N$_2$-atmosphere leads to extensive melt generation. The molten liquid consists of the five phase-fractions—iss, pseudo-tetrahedrite, partially melted galena, an Ag-Sb alloy and bornite.

(4) The Ag in tetrahedrite solid-solution separates out during liquid formation on interaction with galena at 700°C. The released Ag joins the silver-antimonide phase (originally present in the initial concentrate), which results in formation of the Ag-Sb alloy with an approximate composition of 95Ag-5Sb (wt pct).

(5) There is surplus availability of sphalerite in the Garpenberg concentrate, beyond the limits of its assimilation into chalcopyrite. Such limits are dictated by the 700°C-isotherm of iss-phase in the CuS-FeS-ZnS ternary diagram. In such a situation at 700°C, iss-phase demonstrates a tendency to assimilate the extra available Zn (beyond the iss-compositional limits) by precipitating out the Cu-rich bornite phase.

(6) Bornite is the last melt phase-fraction to solidify during cooling of the roasted calcine.

(7) Sphalerite is the major host of trace elements amongst various minerals in the Garpenberg concentrate. It comprises of Mn, Cd and Hg in relatively higher concentrations compared to the other

co-existing sulphide minerals. Galena is the principal host for Tl.

(8) Roasting of the initial concentrate in N_2 atmosphere at 700 °C and subsequent cooling of the roasted calcine result in redistribution of the trace elements. Mn and Tl are found to be segregated in the bornite melt phase-fraction, which is likely the last phase-fraction in the melt to solidify. Cd migrates to the pseudo-tetrahedrite phase. Apparently, the trace elements demonstrate a tendency to segregate into the low-melting phase-fractions inside the cooled and solidified liquids generated during roasting. In contrast, Hg originally present in sphalerite does not exhibit any significant segregation post-roasting, as it evenly spreads out in similar concentrations in all the 5 melt phase-fractions.

(9) The attribute of low-melting liquid phase-fractions to act as a sink, concentrating most of the trace elements during solidification can be useful to formulate new extraction methods for trace elements from the base metal sulphide deposits.

(10) It is demonstrated in this work that sound statistical evaluations can be performed over the data from Laser-Ablation-ICP-MS measurements over sulphide samples, in spite of the challenges in their accurate quantification. The statistical methods such as correlation matrices and clustering analysis could be used effectively to determine insightful sample-related attributes such as the behavior of trace elements initial occurrences and their redistribution consequent to the roasting treatment.

CONFLICT OF INTEREST

On behalf of all authors, the corresponding author states that there is no conflict of interest.

OPEN ACCESS

REFERENCES

1. I. Wilkomirsky, R. Parra, F. Parada, and E. Balladares: in *Conference of Metallurgy 2014*, B. Davis, ed., Metallurigcal and Materials Society, Canada, 2014.
2. Å. Holmström: Ph.D. Thesis, R. Inst. Technol., Dep. Prod. Technol. (Stockholm), 1988.
3. K. Haga, B. Altansukh, and A. Shibayama: *Mater. Trans.*, 2018, vol. 59, pp. 1396–403.
4. S. Shibuya, C. Tokoro, and T. Okura: in *Proc. 7th Eur. Metall. Conf.*, 2013, pp. 111–22.
5. W. Hongu and Z. Lanin: *Int. J. Miner. Process.*, 2016, vol. 153, pp. 1–7.
6. P.R. Taylor and T.A.R. Putra: in *Celebrating Megascale, Proc. Extr. Process. Div. Symp. Pyrometall.*, P.J. Mackey, E.J. Grimsey, R.T. Jones, and G.A. Brooks, eds., John Wiley & Sons, Inc., 2014, pp. 197–211.
7. R. Padilla and M.C. Ruiz: in *Drying, Roasting, Calcining Miner.*, T.P. Battle, J.P. Downey, L.D. May, B. Davis, N.R. Neelameggham, S. Sanchez-Segado, and P.C. Pistorius, eds., Springer International Publishing, Cham, 2016, pp. 43–50.
8. M. Devia, I. Wilkomirsky, and R. Parra: *Mining Metall. Explor.*, 2012, vol. 29, pp. 121–28.
9. A. Bjornberg, S.A. Holmstrom, and G. Lindkvist: in *US Pat. 4,626,279*, 1986.
10. I. Wilkomirsky, F. Parada, A. Ulloa, A. Carrasso, and L. Jeraldo: in *PProc. IV Int. Conf. Clean Technol. Min. Ind.*, vol. 2, Concepción University Press, 1998, pp. 613–21.
11. J.R. Craig and G. Kullerud: *Carnegie Inst. Washingt. Yearb.*, 1967, vol. 65, pp. 344–52.
12. S. Kojima and A. Sugaki: *Miner. J.*, 1984, vol. 12, pp. 15–28.
13. S. Kojima and A. Sugaki: *Econ. Geol.*, 1985, vol. 80, pp. 158–71.
14. K.L. Pruseth, B. Mishra, and H.J. Bernhardt: *Econ. Geol.*, 1997, vol. 92, pp. 720–32.
15. B.R. Frost, J.A. Mavrogenes, and A.G. Tomkins: *Can. Miner.*, 2002, vol. 40, pp. 1–18.
16. G. Stevens, S. Prinz, and A. Rozendaal: *Econ. Geol.*, 2005, vol. 100, pp. 781–86.
17. A.G. Tomkins, B.R. Frost, and D.R.M. Pattison: *Can. Miner.*, 2006, vol. 44, pp. 1045–62.
18. A.G. Tomkins, D.R.M. Pattison, and B.R. Frost: *J. Petrol.*, 2007, vol. 48, pp. 511–35.
19. B. Govindarao, K.L. Pruseth, and B. Mishra: *Ore Geol. Rev.*, 2020, vol. 121(10356), pp. 1–9.
20. B. Govindarao, K.L. Pruseth, and B. Mishra: *Miner. Mag.*, 2020, vol. 84, pp. 859–68.
21. P.N. Prasad, A. Lennartsson, and C. Samuelsson: *Metall. Mater. Trans. B.*, 2020, vol. 51, pp. 1446–59.
22. P.N. Prasad, I. McElroy, A. Lennartsson, and C. Samuelsson: *Metall. Mater. Trans. B.*, 2021, vol. 52, pp. 764–77.

23. P.N. Prasad, A. Lennartsson, and C. Samuelsson: *Metall. Mater. Trans. B.*, 2021, vol. 52, pp. 1866–85.
24. L.J. Cabri, J.L. Campbell, J.H.G. Laflamme, R.G. Leigh, J.A. Maxwell, and J.D. Scott: *Can. Miner.*, 1985, vol. 23, pp. 133–48.
25. N.J. Cook, C.L. Ciobanu, L.V. Danyushevsky, and S. Gilbert: *Geochim. Cosmochim. Acta.*, 2011, vol. 75, pp. 6473–96.
26. N.J. Cook, C.L. Ciobanu, A. Pring, W. Skinner, M. Shimizu, L. Danyushevsky, B. Saini-Eidukat, and F. Melcher: *Geochim. Cosmochim. Acta.*, 2009, vol. 73, pp. 4761–91.
27. N.J. Cook, B. Etschmann, C.L. Ciobanu, K. Geraki, D.L. Howard, T. Williams, N. Rae, A. Pring, G. Chen, and B. Johannessen: *Minerals.*, 2015, vol. 5, pp. 117–32.
28. D.P. Emslie and G.J. Beukes: *Ann. Geol. Surv.*, 1981, vol. 15, pp. 11–28.
29. L. George, N.J. Cook, C.L. Ciobanu, and B.P. Wade: *Am. Miner.*, 2015, vol. 100, pp. 548–69.
30. D.L. Huston, S.H. Sie, G.F. Suter, D.R. Cooke, and R.A. Both: *Econ. Geol.*, 1995, vol. 90, pp. 1167–96.
31. A.C.L. Larocque, J.A. Jackman, L.J. Cabri, and C.J. Hodgson: *Can. Miner.*, 1995, vol. 33, pp. 361–72.
32. J.A. Lockington, N.J. Cook, and C.L. Ciobanu: *Miner. Petrol.*, 2014, vol. 108, pp. 873–90.
33. N.S. McIntyre, L.J. Cabri, W.J. Chauvin, and J.H.G. Laflamme: *Scanning Electron Microsc.*, 1984, pp. 1139–46.
34. L.L. George, N.J. Cook, and C.L. Ciobanu: *Ore Geol. Rev.*, 2016, vol. 77, pp. 97–116.
35. L.L. George, N.J. Cook, and C.L. Ciobanu: *Minerals.*, 2017, vol. 7, p. 17.
36. C. Patten, S.-J. Barnes, E.A. Mathez, and F.E. Jenner: *Chem. Geol.*, 2013, vol. 358, pp. 170–88.
37. Y. Xing, J. Brugger, B. Etschmann, A.G. Tomkins, A.J. Frierdich, and X. Fang: *Nat. Commun.*, 2021, vol. 12, pp. 1–7.
38. S.E. Gilbert, L.V. Danyushevsky, K. Goemann, and D. Death: *J. Anal. At. Spectrom.*, 2014, vol. 29, pp. 1024–33.
39. P.J. Sylvester: in *Laser Ablation-ICP-MS Earth Sc.: Curr. Pract. Outstanding Iisues*, P.J. Sylvester, ed., vol. 40, Mineral. Assoc. Can., 2008.
40. K. Halbach, T. Holbrook, T. Reemtsma, and S. Wagner: *Anal. Bioanal. Chem.*, 2021, vol. 413, pp. 1675–87.
41. S. Theiner, A. Schweikert, S.J.M. Van Malderen, A. Schoeberl, S. Neumayer, P. Jilma, A. Peyrl, and G. Koellensperger: *Anal. Chem.*, 2019, vol. 91, pp. 8207–12.
42. A.D. Ahmed, S.B. Hood, D.R. Cooke, and I. Belousov: *Appl. Comput. Geosci.*, 2020, vol. 8, p. 100036.
43. D. Pozebon, G.L. Scheffler, and V.L. Dressler: *J. Anal. At. Spectrom.*, 2017, vol. 32, pp. 890–919.
44. D. Kutscher, D. Asogan, I. Mudway, P. Brekke, C. Beales, X. Wang, M.W. Perkins, W. Maret, and T.J. Stewart: *Spectroscopy.*, 2020, vol. 35, pp. 16–26.
45. C. Paton, J. Hellstrom, B. Paul, J. Woodhead, and J. Hergt: *J. Anal. At. Spectrom.*, 2011, vol. 26, pp. 2508–18.
46. A. Limbeck, P. Galler, M. Bonta, G. Bauer, W. Nischkauer, and F. Vanhaecke: *Anal. Bioanal. Chem.*, 2015, vol. 407, pp. 6593–617.
47. S.A. Wilson, W.I. Ridley, and A.E. Koenig: *J. Anal. At. Spectrom.*, 2002, vol. 17(4), pp. 406–09.
48. L. Danyushevsky, P. Robinson, S. Gilbert, M. Norman, R. Large, P. McGoldrick, and M. Shelley: *Geochem. Explor. Environ. Anal.*, 2011, vol. 11, pp. 51–60.
49. C. Ballhaus and P. Sylvester: *J. Petrol.*, 2000, vol. 41, pp. 545–61.
50. J. Arif and T. Baker: *Miner. Depos.*, 2004, vol. 39, pp. 523–35.
51. C.C. Wohlgemuth-Ueberwasser, C. Ballhaus, J. Berndt, V. Stotter née Paliulionyte, and T. Meisel: *Contrib. to Mineral. Petrol.*, 2007, vol. 154, pp. 607–17.
52. L.J. Cabri, P.J. Sylvester, M.N. Tubrett, A. Peregoedova, and J.H.G. Laflamme: *Can. Miner.*, 2003, vol. 41, pp. 321–29.
53. J.E. Mungall, D.R.A. Andrews, L.J. Cabri, P.J. Sylvester, and M. Tubrett: *Geochim. Cosmochim. Acta.*, 2005, vol. 69, pp. 4349–60.
54. E.K. Shibuya, J.E.S. Sarkis, J. Enzweiler, A.P.S. Jorge, and A.M.G. Figueiredo: *J. Anal. At. Spectrom.*, 1998, vol. 13, pp. 941–44.
55. J.H. Yuan, X.C. Zhan, C.Z. Fan, L.H. Zhao, D.Y. Sun, Z.R. Jia, M.Y. Hu, and L.J. Kuai: *Fenxi Huaxue/ Chinese J. Anal. Chem.*, 2012, vol. 40(2), pp. 201–07.
56. P. Sylvester: in *Laser Ablation-ICP-MS Earth Sc.: Curr. Pract. Outstanding Iisues*, P.J. Sylvester, ed., vol. 40, Mineral. Assoc. Can., 2008, pp. 67–78.
57. S.E. Gilbert, L.V. Danyushevsky, T. Rodemann, N. Shimizu, A. Gurenko, S. Meffre, H. Thomas, R.R. Large, and D. Death: *J. Anal. At. Spectrom.*, 2014, vol. 29(6), pp. 1042–51.
58. S. Chenery, A. Hunt, and M. Thompson: *J. Anal. At. Spectrom.*, 1992, vol. 7, pp. 647–52.
59. S.P. Kelley and A.E. Fallick: *Geochim. Cosmochim. Acta.*, 1990, vol. 54(3), pp. 883–88.
60. H.R. Kuhn and D. Günther: *Anal. Chem.*, 2003, vol. 75(4), pp. 747–53.
61. M. Guillong, C. Latkoczy, J.H. Seo, D. Günther, and C.A. Heinrich: *J. Anal. At. Spectrom.*, 2008, vol. 23, pp. 1581–89.
62. P.R. Craddock, O.J. Rouxel, L.A. Ball, and W. Bach: *Chem. Geol.*, 2008, vol. 253, pp. 102–13.
63. J. Kosler: in *Laser Ablation-ICP-MS Earth Sc.: Curr. Pract. Outstanding Iisues*, P.J. Sylvester, ed., vol. 40, Mineralogical Association of Canada, 2008, pp. 79–92.
64. M.E. Shaheen, J.E. Gagnon, and B.J. Fryer: *Chem. Geol.*, 2012, vol. 330–331, pp. 260–73.
65. X. Cheng, J. Drozdova, T. Danek, Q. Huang, W. Qi, S. Yang, L. Zou, Y. Xiang, and X. Zhao: *Sustainability.*, 2018, vol. 10, p. 4533.
66. G. Tiu, Y. Ghorbani, N. Jansson, and C. Wanhainen: *Miner. Eng.*, 2021, vol. 167, p. 106889.
67. J. Sandecki and Ö. Amcoff: *Neues Jahrb. für Mineral. Abhandlungen.*, 1981, vol. 141, pp. 324–40.
68. A. Kritikos: Ph.D. Thesis, Uppsala University, Sweden, 2016.
69. F. Di Benedetto, G.P. Bernardini, P. Costagliola, D. Plant, and D.J. Vaughan: *Am. Mineral.*, 2005, vol. 90, pp. 1384–92.
70. N.J. Cook and C.L. Ciobanu: in *Mineral Resources in a Sustainable World, Proceedings of the 13th SGA Biennial Meeting, Nancy, France*, 2015, pp. 24–27.
71. B.J. Wuensch: *Z. Krist. Mater.*, 1964, vol. 119, pp. 437–53.
72. J. Lima-de-Faria: *Croat. Chem. acta.*, 1999, vol. 72, pp. 705–10.
73. J.R. Craig and G. Kullerud: *Carnegie Inst. Wash. Yearb.*, 1967, vol. 65, pp. 344–52.
74. A. Munitz, A. Venkert, P. Landau, M.J. Kaufman, and R. Abbaschian: *J. Mater. Sci.*, 2012, vol. 47, pp. 7955–70.
75. N. Derimow and R. Abbaschian: *Entropy.*, 2018, vol. 20, p. 890.
76. B.R. Frost, S.M. Swapp, and J. Mavrogenes: *Econ. Geol.*, 2011, vol. 106, pp. 869–82.
77. J. Mavrogenes, R. Frost, and H.A. Sparks: *Can. Mineral.*, 2013, vol. 51, pp. 841–50.
78. S.N. Hoda and L.L.Y. Chang: *Am. Miner. J. Earth Planet. Mater.*, 1975, vol. 60, pp. 621–33.
79. I. V Veksler and B. Charlier: in *Layered intrusions*, B. Charlier, O. Namur, R. Latypov, and C. Tegner, eds., Springer Geology, 2015, pp. 229–58.
80. L.T. Bryndzia and O.J. Kleppa: *Am. Miner.*, 1988, vol. 73, pp. 707–13.
81. L.T. Bryndzia and O.J. Kleppa: *Geochim. Cosmochim. Acta.*, 1988, vol. 52, pp. 167–76.
82. T. Tsujimura and A. Kitakaze: *Neues Jahrb. Miner. Monatsh.*, 2004, pp. 433–44.
83. A. Imai, L.O. Suerte, and S. Nishihara: *Resour. Geol.*, 2009, vol. 59, pp. 307–13.
84. N.E. Johnson, J.R. Craig, and J.D. Rimstidt: *Am. Miner.*, 1988, vol. 73, pp. 389–97.
85. L. Pierce and P.R. Buseck: *Am. Mineral.*, 1978, vol. 63, pp. 1–16.